OBSERVABILITY METRICS FOR SPACE-BASED CISLUNAR DOMAIN AWARENESS

Erin E. Fowler* **and Derek A. Paley†**

ABSTRACT

This paper analyzes orbit families for the mission of space-based cislunar domain awareness and evaluates a novel set of metrics that can be used to inform the specific orbit parameterization for cislunar SDA constellation design. We present a dynamic simulation of the cislunar environment for use in numerical analysis of various pairings of resident space objects and sensing satellites intended for cislunar space domain awareness. Then we apply numerical observability analysis to calculate the local estimation condition number of observations of satellites on trajectories in the Earth-Moon system. Using our catalogue of simulated cislunar orbits as well as our heuristic and empirical metrics, we describe which orbit families provide the best observability of other cislunar orbit families and suggest a method for architecting constellations of observers in different cislunar orbits to perform the general cislunar space domain awareness mission.

INTRODUCTION

Space domain awareness (SDA) and space traffic management (STM) are challenging due to an increasingly congested environment populated by a growing number of maneuverable vehicles and vehicles planned for deep space, i.e., beyond geosynchronous Earth orbit (GEO). Orbit design for the space-based cislunar domain awareness mission is an important topic due to the large range and limited viewing geometries between Earth-orbiting satellites and satellites in cislunar orbits. Complex astrodynamics must be modeled for objects in cislunar space, since lunar gravity cannot be neglected or treated as a perturbation to a dynamic model for cislunar object tracking as in dynamic models of Earth-orbiting vehicles.

The cislunar regime is of increasing interest to the space industry due to its value for applications such as astronomy, interplanetary mission staging, lunar exploration and communications, and Earth orbit insertion.[1] Spacecraft placed in Earth-Moon collinear Lagrange points L1 and L2 avoid the gravity wells of the Earth and Moon, surface environmental issues, and artificial and natural space debris. These spacecraft require low station-keeping propellant (on the order of

*PhD Candidate, Department of Aerospace Engineering, University of Maryland, 8197 Regents Drive, Room 1141, College Park, MD 20742, efowler3@umd.edu.

†Willis H. Young Jr. Professor of Aerospace Engineering Education, Department of Aerospace Engineering and Institute for Systems Research, University of Maryland College Park, 3150 Glenn L. Martin Hall, College Park, MD 20742, dpaley@umd.edu.

meters or tens of meters per second per year)[2] and can travel with low propellant cost between L1 and L2 or between Earth-Moon space and Sun-Earth space.[3]

In July 2019, a near-rectilinear halo orbit (NRHO) about Earth-Moon L2 was chosen as the orbit for the future Lunar Gateway, which will be developed by the U.S. National Aeronautics and Space Administration (NASA) and the European Space Agency (ESA) to serve as a solar-powered communications hub, science laboratory, short-term habitation module, and holding area for rovers and other robots.[1] Cislunar orbits can also be used as storage locations for spare Earth-orbiting satellites, allowing responsive insertion of these spares into operational Earth orbits with none of the indications and warnings normally associated with launch of a new vehicle into Earth orbit.[4] However, despite the desirable characteristics of certain cislunar orbits, NASA's ARTEMIS P1 (THEMIS B) and ARTEMIS P2 (THEMIS C) were the first two satellites to achieve orbit around an Earth-Moon Lagrange point in 2010.[5] As the opportunities offered by the cislunar regime become realities in the near future, space domain awareness and space traffic management specific to this environment will become increasingly critical capabilities. Preliminary results from this study could be used to inform the requirements for future cislunar space domain awareness systems, i.e., by placing satellites into specific orbits and constellations that maximize performance for SDA and STM missions.

Various models describe motion in the Earth-Moon system, including approaches using patched conics by switching among two-body models with the Earth, the Sun, and the Moon as central bodies; three-body models including the Earth and the Moon as primary masses; n-body models that directly incorporate the gravitational effects from more bodies than the two primaries; and models that incorporate perturbations like solar radiation pressure. A three-body model, which is used here, may be derived from a set of simplifying assumptions. The restricted three-body problem assumes that a body of negligible mass moves under the influence of two massive bodies. The circular restricted three-body problem additionally assumes that the two primary masses move in nearly circular orbits about their barycenter. For the Earth-Moon system, these assumptions are valid since a large spacecraft of 5900 kg would exert less than 10^{-16} times the force on the primaries than the primaries would exert on each other, and the Moon's orbit has an eccentricity of only 0.055.[6] The Circular Restricted Three-Body Problem (CR3BP) is used here as the basis for a dynamic simulation in which the relative motion of two or more satellites of negligible mass is studied.

Our approach to studying space-based observability in the Earth-Moon system begins with the development of a catalog of trajectories representing a range of Earth and Moon orbits propagated in the Earth-Moon system, Earth-Moon L1 and L2 Lyapunov orbits (closed trajectories that remain in the plane of the Earth-Moon system), Earth-Moon L1 and L2 halo orbits (closed trajectories that include an out-of-plane component with respect to the Earth-Moon system and are controlled to maintain matching in-plane and out-of-plane frequencies), and in-plane Earth-Moon L4 orbits. Using this catalog of trajectories in the Earth-Moon system, we make various pairings to represent observer and target trajectories, where an observer trajectory can be any trajectory in the catalog, and target trajectories are restricted to be Lagrange point orbits only (L1, L2, L4). By studying the evolution of the relative geometries of these pairings

over time and adding one year of Sun ephemeris from the Jet Propulsion Laboratory (JPL) Horizons database,[7] we are able to calculate several heuristic metrics of interest to space-based cislunar domain awareness missions. For instance, we calculate how long it would take the target object to pass through an angular unit of the observer's field of view, how often the target object would be hidden behind the Earth or the Moon from the perspective of the observer, how often the observer may not be able to point an optical sensor at the target due to a Sun exclusion angle, and the range from the observer to the target, which could be used to determine (for instance) signal-to-noise ratio for an optical sensor given a specific target size and illumination.

After reviewing these heuristic metrics for space-based observability in the Earth-Moon system, we then apply a numerical observability analysis technique, which adds further understanding to pairings of one observer with one target and permits consideration of multiple observers in different trajectories observing a single target. Krener and Ide offer a method for calculating the empirical local observability gramian matrix based on the nominal initial state of the target trajectory, as well as perturbed versions of this initial state with their corresponding output.[8] We take the common logarithm of the condition number of this gramian and use it to compare observability for measurements of a target trajectory from chosen observer trajectories; a smaller condition number represents better observability. We choose the measurement to be the vector from the observer to the target. Our first set of results includes average values for this metric across all observer trajectories in each family. That is, a result for the Earth-orbiting observer family is the average of this condition number for Earth-orbiting observer trajectories across a range of semi-major axes, eccentricities, and inclinations.

To consider observability when a two-observer constellation may observe a single target, we choose the measurement to be the vectors from each observer to the target. Our second set of results, for constellations of observers rather than single observers, includes the condition number for this gramian based on the nominal observer trajectory from the orbit family in question rather than an average across all trajectories in the family. For example, the nominal Earth-orbiting trajectory has the nominal semi-major axis, eccentricity, and inclination as defined in our catalog of cislunar trajectories. The empirical observability metric takes into account the dynamics of the system as well as its geometry.

In closely related prior work, Knister applied model-based systems engineering to assess the performance and financial burden of a given system of SDA sensors based on CR3BP dynamics.[9] Knister's Mean Detect Time (MDT) is the ratio of the time during which the object of interest can be detected and the total time of the simulation. In order to evaluate whether or not an object can be detected, MDT incorporates a lower threshold for signal-to-noise ratio (SNR) based on illumination, whereas our comparable metric (inavailability) includes information on whether or not a target object is obscured by the Moon or Earth from the perspective of the observer or within a Sun exclusion angle from the perspective of the observer, without considering target object illumination. Additionally, Knister does not consider our range and angular interval metrics in his evaluation, and we do not consider tracking or cost metrics.

Whereas we evaluate target objects in L1 and L2 halo orbits, L1 and L2 Lyapunov orbits, and L4 planar orbits, Knister only evaluates target objects in L1 Lyapunov orbits. Furthermore, we evaluate observers in these L1, L2, and L4 orbits, as well as Keplerian Earth and Moon orbits, whereas Knister evaluates observers in Earth orbits only (various LEO and GEO). Using the local estimation condition number, we are additionally able to analyze cases with multiple observers as well as single observers.

The contributions of this paper are (1) evaluation of the estimation performance of cislunar orbits from an observing cislunar, lunar, or Earth orbit using nonlinear observability theory; (2) pairwise analysis of target and observer orbits spanning Keplerian and Lagrangian orbit families, comparing our nonlinear observability metric with heuristics like range, inavailability, and angular interval; and (3) evaluation of the estimation performance of constellations of two observers against cislunar targets. A preliminary version of this paper appeared at the 31st AAS/AIAA Space Flight Mechanics Meeting in February 2021. The empirical observability results for multiple observers have not appeared previously.

The outline of the paper is as follows. The next section provides background information on cislunar dynamics, including a description of the circular restricted three-body problem (CR3BP), calculations of the locations and stability characteristics of the five equilibrium (Lagrange) points in the CR3BP, a discussion of the types of periodic motions that can be found about Lagrange points in the Earth-Moon system, and an explanation of some of the challenges to cislunar space domain awareness. The following section describes the ways in which we have quantified the observability of cislunar trajectories using heuristic and theoretically justified metrics from numerical observability. Next, we provide results representing how various observer-target trajectory pairings fare against our heuristic and observability metrics. Finally, we provide results representing how constellations of two observers perform using the empirical observability metric given a target in an L1 Lyapunov trajectory.

CISLUNAR DYNAMICS

The Circular Restricted Three-Body Problem

Motion within the Earth-Moon system may be approximated using the dynamics of the Circular Restricted Three-Body Problem (CR3BP), in which the motion of a spacecraft with negligible mass is modeled under the influence of the gravitation of two primaries approximated as point masses.[10] By convention, the motion of the spacecraft is described using a coordinate system that rotates with the rate of rotation of the two primary masses in circular orbits about their barycenter. The planar CR3BP has two degrees of freedom, whereas the spatial CR3BP has three. Only one constant of motion exists, known as the Jacobi integral.[10]

Since the position of the center of mass of the system $\mathbf{r}_{CM} = \frac{m_1\mathbf{r}_1+m_2\mathbf{r}_2}{m_1+m_2} = \mathbf{0}$, the distance of the first primary from the origin $r_1 = \frac{-m_2 r_2}{m_1} = \frac{-m_2}{m_1}(r_{12}+r_1)$, where $r_{12} = r_1 + r_2$ is the constant distance between the two primaries m_1 and m_2, and the distance of the second primary from the origin $r_2 = \frac{m_1}{m_1+m_2} r_{12}$. The acceleration of m_2 is $m_2\omega^2\mathbf{r}_2$.

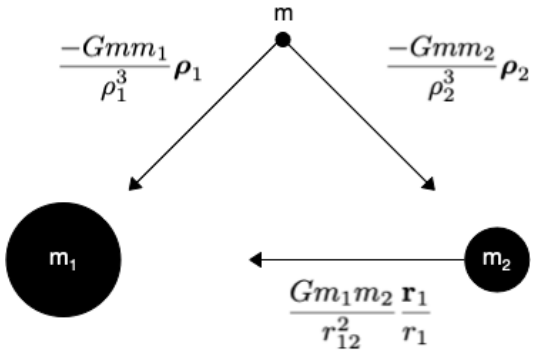

Figure 1: Free-body diagrams of spacecraft m (top) and smaller primary mass m_2 (right). $\boldsymbol{\rho}_1$ and $\boldsymbol{\rho}_2$ are the vectors from the spacecraft m to the first primary m_1 and the second primary m_2, respectively.

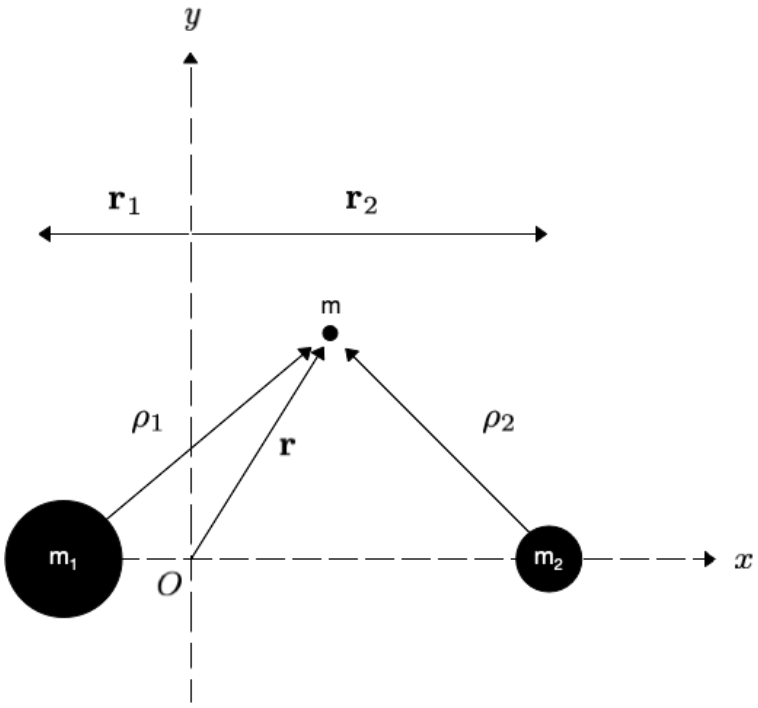

Figure 2: Circular Restricted Three-Body Problem. Mass m is a spacecraft of negligible mass compared to $m_1 \geq m_2$, which are two large primary masses.

The free-body diagram for m_2 shown in Figure 1 gives $\frac{Gm_1m_2}{r_{12}^2} = m_2r_2\omega^2 = \frac{m_1m_2}{m_1+m_2}r_{12}\omega^2$, which implies that the system shown in Figure 2 rotates at an angular rate of[11]

$$\omega = \sqrt{\frac{G(m_1+m_2)}{r_{12}^3}}. \tag{1}$$

The free-body diagram for the spacecraft m in Figure 1 provides the basis for the equations of motion in the CR3BP. The inertial acceleration is $\mathbf{a}_i = \mathbf{a}_0 + \ddot{\mathbf{r}} + 2\boldsymbol{\omega} \times \mathbf{v} + \dot{\boldsymbol{\omega}} \times \mathbf{r} + \boldsymbol{\omega} \times (\boldsymbol{\omega} \times \mathbf{r})$, where $\mathbf{a}_0 = \mathbf{0}$ is the translational acceleration

of the rotating frame, $2\boldsymbol{\omega} \times \mathbf{v}$ is the Coriolis acceleration, $\dot{\boldsymbol{\omega}} = \mathbf{0}$ is the time derivative of $\boldsymbol{\omega}$, and $\boldsymbol{\omega} \times (\boldsymbol{\omega} \times \mathbf{r})$ is the centripetal acceleration. We have

$$\ddot{\mathbf{r}} = \mathbf{a}_i - 2\boldsymbol{\omega} \times \mathbf{v} - \boldsymbol{\omega} \times (\boldsymbol{\omega} \times \mathbf{r}). \tag{2}$$

Newton's second law gives $\mathbf{a}_i = -G\left(\frac{m_1}{\rho_1^3}\boldsymbol{\rho}_1 - \frac{m_2}{\rho_2^3}\boldsymbol{\rho}_2\right)$, with $\boldsymbol{\rho}_1 = \mathbf{r} - \mathbf{r}_1 = \begin{bmatrix} x + \frac{m_2 r_{12}}{m_1+m_2} & y & z \end{bmatrix}^T$ and $\boldsymbol{\rho}_2 = \mathbf{r} - \mathbf{r}_2 = \begin{bmatrix} x - \frac{m_1 r_{12}}{m_1+m_2} & y & z \end{bmatrix}^T$. The CR3BP rotates about the z axis in the frame shown in Figure 2 (by convention in the $+z$ direction), giving $\boldsymbol{\omega} = \begin{bmatrix} 0 & 0 & \omega \end{bmatrix}^T$. Therefore Equation 2 becomes

$$\ddot{\mathbf{r}} = \frac{-Gm_1}{||\mathbf{r} - \mathbf{r}_1||}\begin{bmatrix} x + \frac{m_2}{m_1+m_2}r_{12} \\ y \\ z \end{bmatrix} - \frac{Gm_2}{||\mathbf{r} - \mathbf{r}_2||}\begin{bmatrix} x - \frac{m_1}{m_1+m_2}r_{12} \\ y \\ z \end{bmatrix} + 2\omega\begin{bmatrix} \dot{y} \\ -\dot{x} \\ 0 \end{bmatrix} + \omega^2\begin{bmatrix} x \\ y \\ 0 \end{bmatrix}. \tag{3}$$

By convention, position, velocity, and mass are nondimensionalized in the CR3BP, so that the distance r_{12} between the Earth and the Moon becomes unity.[11] The Earth's mass is denoted $1 - \mu$ and the Moon's mass is μ. One distance unit is defined as $1DU \equiv r_{12}$, one mass unit as $1MU \equiv m_1 + m_2$ (so that mass ratio is $\mu = \frac{m_2}{m_1+m_2}$), and one time unit as $1TU \equiv \frac{T}{2\pi}$, where the orbital period T of the primaries about their barycenter is $T = \frac{2\pi}{\omega} = 2\pi\sqrt{\frac{r_{12}^3}{G(m_1+m_2)}}$ (a sidereal month).[12]

Using this nondimensionalization, the equations of motion for a spacecraft of negligible mass m from Equation 3 become[12]

$$\begin{bmatrix} \ddot{x} \\ \ddot{y} \\ \ddot{z} \end{bmatrix} = -\frac{(1-\mu)}{\rho_1^3}\begin{bmatrix} x + \mu \\ y \\ z \end{bmatrix} - \frac{\mu}{\rho_2^3}\begin{bmatrix} x - 1 + \mu \\ y \\ z \end{bmatrix} + \begin{bmatrix} 2\dot{y} \\ -2\dot{x} \\ 0 \end{bmatrix} + \begin{bmatrix} x \\ y \\ 0 \end{bmatrix}. \tag{4}$$

Table 1: Constants used for nondimensionalizing the Earth-Moon system

Unit	Variable	Value
Earth-Moon system orbital period	T	27.3215 days
Time unit	TU	4.348 days
Distance unit	DU	384400 km
Speed unit	SU	1.023 km/s
Mass ratio	μ	0.012277471

By convention, a state in the system with a positive ($+z$) angular momentum (such that the spacecraft is moving counter-clockwise in the Earth-Moon rotating frame) is considered prograde, whereas a clockwise motion is considered retrograde.[13] A solution in the CR3BP can be one of four types:[14] an equilibrium point, a periodic orbit (Lyapunov or halo), a quasi-periodic orbit (Lissajous), and chaotic motion.

Equilibrium Points in the CR3BP

At equilibrium points in the CR3BP (known as Lagrange or libration points), gravitational forces and rotational accelerations are balanced.[12] At stable equilibrium points, perturbations cause oscillations about the equilibrium point, whereas at unstable equilibrium points, perturbations cause drift away from the equilibrium point. Collinear Lagrange points L1, L2, and L3 are saddle points; there is a family of periodic orbits surrounding each of these points. The planar periodic orbits are called Lyapunov orbits and their three-dimensional counterparts are called halo and Lissajous orbits.[10] The z-axis solution to the linear part of Equation 3, obtained by setting $x = 0$ and $y = 0$, is simple harmonic. Linearized analysis of the coupled xy behavior of Equation 3 further reveals two real roots of opposite sign and two imaginary roots. Since the two real roots are opposite in sign, arbitrarily chosen initial conditions give rise to unbounded solutions as time increases, but if initial conditions are restricted such that only the non-divergent mode is allowed, the coupled motion in the xy plane is bounded and periodic.[10]

Consider the pseudopotential $U = \frac{1}{2}\omega^2(x^2 + y^2) + \frac{1-\mu}{\rho_1} + \frac{\mu}{\rho_2}$. Equilibrium points occur where the gradient of the pseudopotential U vanishes.

Note that

$$\begin{bmatrix} \ddot{x} \\ \ddot{y} \\ \ddot{z} \end{bmatrix} = \begin{bmatrix} 2\omega\dot{y} + \frac{\partial U}{\partial x} \\ -2\omega\dot{x} + \frac{\partial U}{\partial y} \\ \frac{\partial U}{\partial z} \end{bmatrix}. \tag{5}$$

When a spacecraft is at rest at an equilibrium point, $\dot{x} = \ddot{x} = \dot{y} = \ddot{y} = \dot{z} = \ddot{z} = 0$, which implies $\frac{\partial U}{\partial x} = \frac{\partial U}{\partial y} = \frac{\partial U}{\partial z} = 0$. Since $\frac{\partial U}{\partial z} = -z\mu((x - 1 + \mu)^2 + y^2 + z^2)^{-\frac{3}{2}}$, then $z = 0$ is the only solution of $\frac{\partial U}{\partial z} = 0$, meaning that all Lagrange points lie in the xy plane of the rotating frame defined in Figure 2.[11]

Using U in terms of μ, ρ_1, and ρ_2, trivial solutions to $\frac{\partial U}{\partial x} = \frac{\partial U}{\partial \rho_1}\frac{\partial \rho_1}{\partial x} + \frac{\partial U}{\partial \rho_2}\frac{\partial \rho_2}{\partial x} = 0$ and $\frac{\partial U}{\partial y} = \frac{\partial U}{\partial \rho_1}\frac{\partial \rho_1}{\partial y} + \frac{\partial U}{\partial \rho_2}\frac{\partial \rho_2}{\partial y} = 0$ may be found. When $\frac{\partial U}{\partial \rho_1} = (1 - \mu)\left(\rho_1 - \frac{1}{\rho_1^2}\right)$ and $\frac{\partial U}{\partial \rho_2} = \mu\left(\rho_2 - \frac{1}{\rho_2^2}\right)$ are set to 0, $\rho_1 = \rho_2 = 1$, meaning that the distances from the primaries to the spacecraft are the same and also equal to the distance between the primaries, forming an equilateral triangle. These points are known as L4 and L5.[11]

Stating $x^2 + y^2$ in terms of μ, ρ_1, and ρ_2, the pseudopotential becomes

$$U = (1 - \mu)\left(\frac{\rho_1^2}{2} + \frac{1}{\rho_1}\right) + \mu\left(\frac{\rho_2^2}{2} + \frac{1}{\rho_2}\right) - \frac{\mu(1 - \mu)}{2}. \tag{6}$$

To define the locations of the remaining equilibrium points (L1, L2, and L3), full solutions for $\frac{\partial U}{\partial x}$ and $\frac{\partial U}{\partial y}$ (and thus for $\frac{\partial \rho_1}{\partial x}$, $\frac{\partial \rho_1}{\partial y}$, $\frac{\partial \rho_2}{\partial x}$, $\frac{\partial \rho_2}{\partial y}$) are required. Given $\frac{\partial \rho_1}{\partial y} = \frac{y}{\rho_1}$ and $\frac{\partial \rho_2}{\partial y} = \frac{y}{\rho_2}$, the solution $\frac{\partial U}{\partial y} = (1 - \mu)\left(\rho_1 - \frac{1}{\rho_1^2}\right)\left(\frac{y}{\rho_1}\right) + \mu\left(\rho_2 - \frac{1}{\rho_2^2}\right)\left(\frac{y}{\rho_2}\right) = 0$ reveals that $y = 0$ for the remaining equilibrium points L1, L2, and L3, described as the collinear Lagrange points because they are on the line drawn between the Earth and the Moon (the x axis in the CR3BP synodic frame). Given $\frac{\partial \rho_1}{\partial x} = \frac{x+\mu}{\rho_1}$ and $\frac{\partial \rho_2}{\partial x} = \frac{x-1+\mu}{\rho_2}$, the positions of L1, L2, and L3 along the x axis are

found from the solution $\frac{\partial U}{\partial x} = (1-\mu)\left(\rho_1 - \frac{1}{\rho_1^2}\right)\left(\frac{x+\mu}{\rho_1}\right) + \mu\left(\rho_2 - \frac{1}{\rho_2^2}\right)\left(\frac{x-1+\mu}{\rho_2}\right) = 0$, i.e.,

$$\begin{aligned} x_{L1} &= (1-\mu) - \rho_2 \\ x_{L2} &= \rho_2 + (1-\mu) \\ x_{L3} &= -\rho_1 - \mu. \end{aligned} \tag{7}$$

The solutions to Equation 7 are found numerically as functions of mass ratio μ.[14] See Figure 3 for a depiction of the geometry of the Lagrange points.

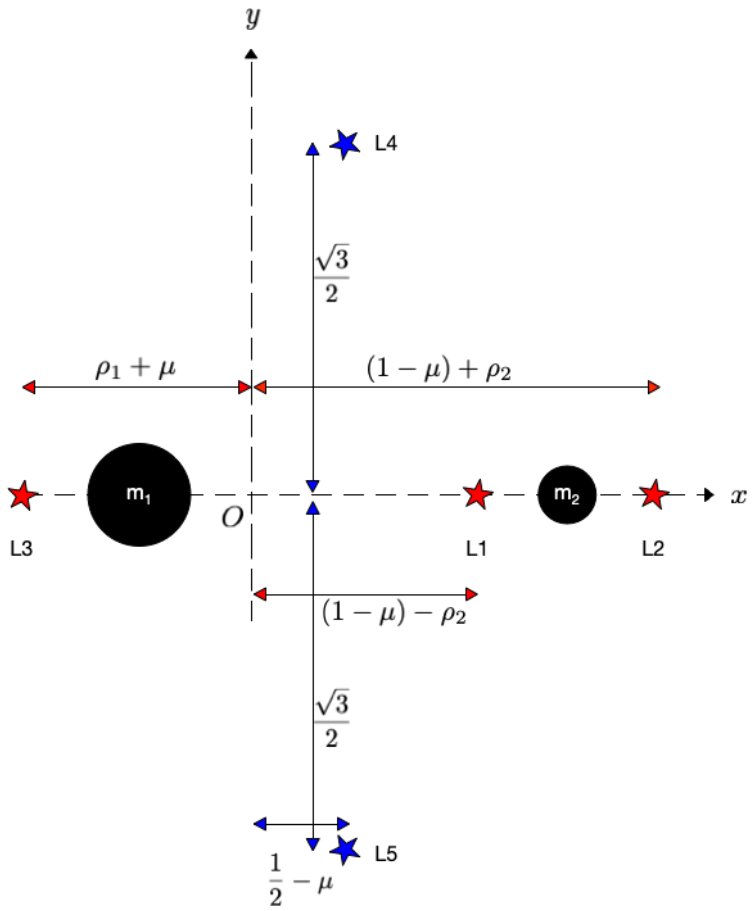

Figure 3: Locations of Lagrange points for the CR3BP. L4 and L5 are stable equilibrium points, whereas L1, L2, and L3 are saddle points.

Cislunar Orbits

Lyapunov orbits and halo orbits are periodic motions about the collinear Earth-Moon Lagrange points (L1, L2, L3). Lyapunov orbits lie entirely in the plane of the two primary bodies (the xy plane shown in Figure 2), whereas halo orbits include an out-of-plane component. L1 Lyapunov orbits, L2 Lyapunov orbits, and L4 planar orbits considered in this analysis are shown in Figure 4. Halo orbits considered in this analysis are shown in Figure 5. Orbits about

the Earth-Moon L2 point are called halo orbits when the size of the orbit is comparable to the distance to L2 from the Moon, resulting in periodic three-dimensional motion, and when controlled such that the frequency of the out-of-plane motion matches that of the in-plane motion. An L2 halo orbit requires relatively low $Delta$-velocity (ΔV) to reach from Earth and, with sufficiently large amplitude, it allows continuous Earth visibility, appearing as an elliptical motion around the Moon from the perspective of the Earth .[13]

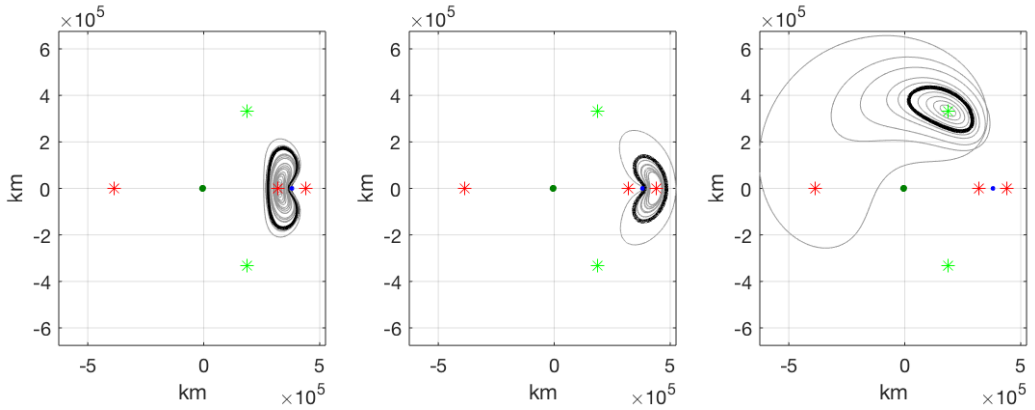

Figure 4: Visualizations in the Earth-Moon plane of (from left to right) the L1 and L2 Lyapunov and L4 planar orbits described in Table 2 with the nominal orbits in bold. The Earth (green) and Moon (blue) are shown to scale in the appropriate locations. The range of orbit periods shown for L1 orbits is 13.1–28.6 days, for L2 orbits 14.8–31.1 days, and for L4 orbits 27.5–28.7 days.

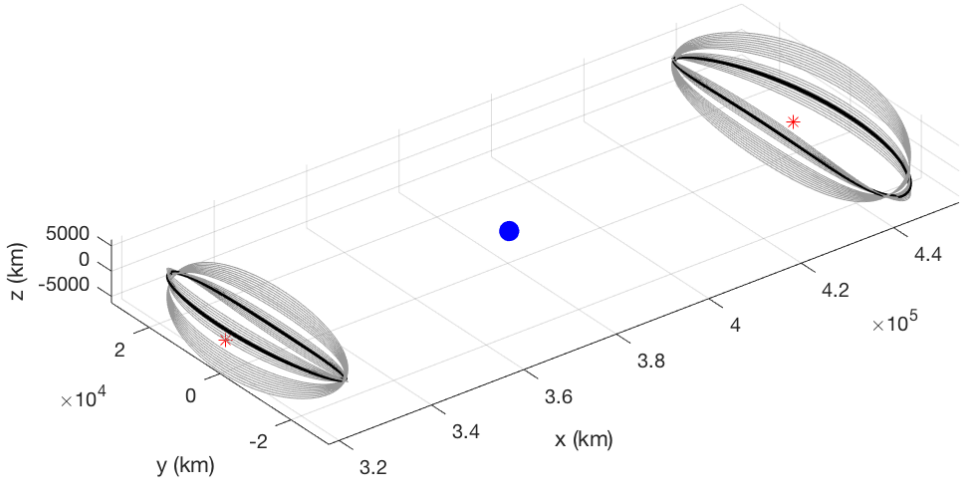

Figure 5: Visualization of the range of L1 and L2 halo orbits described in Table 2, with the nominal orbits in bold. Class I halos tilt in the $-x$ direction toward the Earth (not pictured), whereas Class II halos tilt in the $+x$ direction. The Moon is shown to scale in the appropriate location. The L1 halo orbit period is $\sim \mathbf{12.5}$ days, and the L2 halo orbit period is $\sim \mathbf{14.7}$ days.

Challenges for Cislunar Space Domain Awareness

Objects in cislunar orbits are approximately ten times farther from the Earth's surface than objects being tracked in geostationary or geosynchronous earth orbits (GEO/GSO).[15] Given current technology, optical systems based on the Earth's surface are capable of detecting only very large objects at those distances because signal-to-noise ratio is so greatly reduced at that range. Deep-space missions for science and exploration have used cooperative methods for orbit determination (e.g., two-way Doppler tracking) at these and larger ranges, but for space domain awareness and space traffic management purposes, cooperative methods cannot be assumed.[16] Additionally, objects in cislunar space appear to move very slowly from the perspective of an observer based on the Earth's surface or even orbiting the Earth, such that there may be insufficient geometric diversity in the observations for the observer to detect motion and create an orbit estimate, whether a detection is defined as a streak across a focal plane or a time-stamped series of collections against an unresolved point. Objects in the cislunar environment can also spend significant time in front of or behind the Moon or the Earth, or within a Sun- or Moon-exclusion angle with respect to an observer's sensor, which could cause an observer to lose custody of the object. These considerations form the basis for the heuristic metrics proposed below. However, these metrics are limited because they do not consider the underlying dynamics of the system, which motivates the use of observability as described next.

QUANTIFYING THE OBSERVABILITY OF CISLUNAR ORBITS

Application of Observability Gramian to Cislunar Orbits

To investigate the cislunar space domain awareness and orbit determination problem in cases when it is of interest to find a degree of observability rather than a binary result describing only whether or not a phenomenon is observable, a numerical method is used.[8] The observability gramian measures the sensitivity of a chosen measurement or output to the initial conditions of the system. The local observability gramian is defined as

$$P(x^0) = \int_0^T \Phi'(t)H'(t)H(t)\Phi(t)dt, \tag{8}$$

where Φ is the fundamental matrix solution of the linear dynamics and H is the measurement Jacobian. Prime $'$ denotes the transpose of a matrix. Computing this gramian is difficult because it requires computation of Φ and H. Krener and Ide offer a method for calculating the (i,j) components of the $n \times n$ empirical local observability gramian matrix $P(\mathbf{x}^0)$:

$$P(\mathbf{x}^0)_{(i,j)} = \frac{1}{4\epsilon^2}\int_0^T (\mathbf{y}^{+i}(t) - \mathbf{y}^{-i}(t))'(\mathbf{y}^{+j}(t) - \mathbf{y}^{-j}(t))dt, \tag{9}$$

where $\mathbf{x}^0$ is the nominal initial state of the target trajectory, $\mathbf{x}^{\pm i} = \mathbf{x}^0 \pm \epsilon\mathbf{e}^i$ and $\mathbf{y}^{\pm i}(t)$ are the perturbed state and corresponding output, $\epsilon > 0$ is a small displacement, and $\mathbf{e}^{i=1,\ldots,n}$ is the ith unit vector in the real coordinate space of n dimensions $\mathbb{R}^n$.[8] The condition number for the resulting matrix is the ratio of the largest local singular value to the

smallest; a large condition number indicates that the estimation problem is ill-conditioned for the given states, whereas a small condition number equates to better observability.[17] If the observed dynamical system is smooth, meaning that all partial derivatives exist and are continuous, then this gramian converges to the local observability gramian for $\epsilon \to 0$.[8] Computing the empirical gramian requires only the ability to simulate the observed dynamical system.[8]

In order to apply the empirical observability metric, we start by loading an observer trajectory from our catalog and defining initial conditions $\mathbf{x}_{0,tar}$ for the 6×1 target state. Additionally, we define a time step t_{step} and a small perturbation $\epsilon = 0.0001$. We then define 12 perturbed initial condition vectors $\mathbf{x}_{0+i}$ and $\mathbf{x}_{0-i}$, $i = 1, \ldots, 6$, which represent initial conditions perturbed in the positive and negative directions by ϵ in the position components and by $\frac{2\pi\epsilon}{T}$ in the velocity components (so that perturbation ϵ has a properly scaled effect on velocity as compared to its effect on position). We propagate these initial conditions using the CR3BP dynamics in Equation 4. We then find measurements $\mathbf{y}$ from the observer trajectory to the trajectories resulting from the 12 perturbed initial condition vectors for the target. We calculate $\mathbf{y}$ at each time step as a 4×1 vector composed of the 3×1 unit vector direction to the target from the observer concatenated with the scalar range between target and observer, separating the range and unit vector in this way to aid the intuitive understanding of the resulting values. Future work could include calculations of $\mathbf{y}$ to represent angles-only measurements like those resulting from electro-optical sensor collections. Finally, we use Equation 9 with a Riemann sum approximation of the integral over our finite time steps to calculate the components of the 6×6 empirical local observability gramian. We use Matlab's `cond` function to find the condition number of the gramian, and we take the common logarithm of this condition number to find our final empirical observability metric as shown in Figure 7.

Heuristic Observability Metrics

In order to use a CR3BP dynamic simulation to analyze various orbit pairings, we additionally define several heuristic observability metrics. Since an estimate of the trajectory of an object is based on observations, the object must have some apparent motion with respect to the observer.[18] For instance, better orbit estimates result from more diverse line of sight measurements. Our first metric is the inverse of the relative angular rate, defined as time per degree of motion of the observed object from the perspective of the observer, assuming a uniformly sensed field of view. A lower value for this metric represents a more observable orbit. This metric is calculated by first taking an in-plane angle (designated IP) and an out-of-plane angle (designated OP) to the target object from the observer, with respect to the Earth-Moon synodic frame. The in-plane angle (IP) is calculated as the anticlockwise angle between the $+x$ axis and the projection of the vector from the observer to the target onto the xy plane. The out-of-plane angle (OP) is the angle between the $+x$ axis and the projection of the vector from the observer to the target onto the xz plane. The angle of interest is the angle through which the target passes from the perspective of the observer in a single simulation time step, calculated as $d\theta = \sqrt{(dIP\cos(OP))^2 + dOP^2}$. In most cases we use the small angle approximation and

assume $\cos(OP) \approx 1$ since our trajectories remain in or near the xy plane. In cases that include out-of-plane motion and an observer-target pairing near the same Lagrange point, we include the $\cos(OP)$ term. We take the average value of $\frac{d\theta}{dt}$, with simulation time step one hour, over the entire simulation time (one year), and the inverse of this average is the metric result that appears in Figure 7.

Other viewing geometry concerns, like occultation by the Earth or Moon and Sun exclusion angles for optical sensors, reduce the amount of time that an object of interest is viewable by the observer. Therefore, the second metric is the percentage of the simulation time during which the target object is unavailable to the observer for any of these reasons. A lower value for this metric represents a more observable orbit. Earth and Moon positions and sizes are directly available in the CR3BP simulation, and we include the Sun's position by assuming a mission start date of January 1, 2010 and using downloaded Sun ephemeris data with respect to the Earth-Moon barycenter from the JPL Horizons database (`https://ssd.jpl.nasa.gov/horizons.cgi`). Figure 6 depicts the Moon in its various phases and the way that the Sun-Earth-Moon geometry evolves over time with these phases. The same figure also depicts the types of inavailability that we have considered in our analysis, including obscuration of a target by the Earth and the Moon (represented by a depiction of obscuration of a target by the Moon on the left side of the figure) and placement of a target within a 30^o sun exclusion angle (depicted on the right side of the figure). Here, we have considered a target obscured by the Earth or Moon if it is either in front of or behind the Earth or Moon from the perspective of the observer, but we did not include Earth or Moon exclusion angles larger than their physical extent, which might be relevant for both electro-optical and radio frequency sensors.

Finally, we consider the range between the observer and the object being observed. Target range affects different sensors in different ways. Signal-to-noise ratio for an optical sensor decreases as the square of the range; received power for radar decreases as the fourth power of the range. However, regardless of sensor phenomenology, large range will negatively affect performance for a cislunar SDA mission. Since objects in orbit around or near the Moon are approximately ten times farther from Earth than the farthest objects being tracked in other space domain awareness efforts (i.e., objects in GEO), range is a critical third metric that can be reduced by prudent placement of space-based assets.

While metrics from numerical observability are theoretically justified and thus the emphasis of ongoing work, supplementing early analysis with heuristic metrics has allowed for a more intuitive understanding of the cislunar system and validation of the observability results.

PERFORMANCE EVALUATION OF CISLUNAR OBSERVING ORBITS

Performance Evaluation of a Single Cislunar Observing Orbit

Table 2 shows the orbit families and parameters considered in this analysis. The target objects in this analysis were placed in trajectories according to the nominal value of each parameter for the given family and the observer orbits

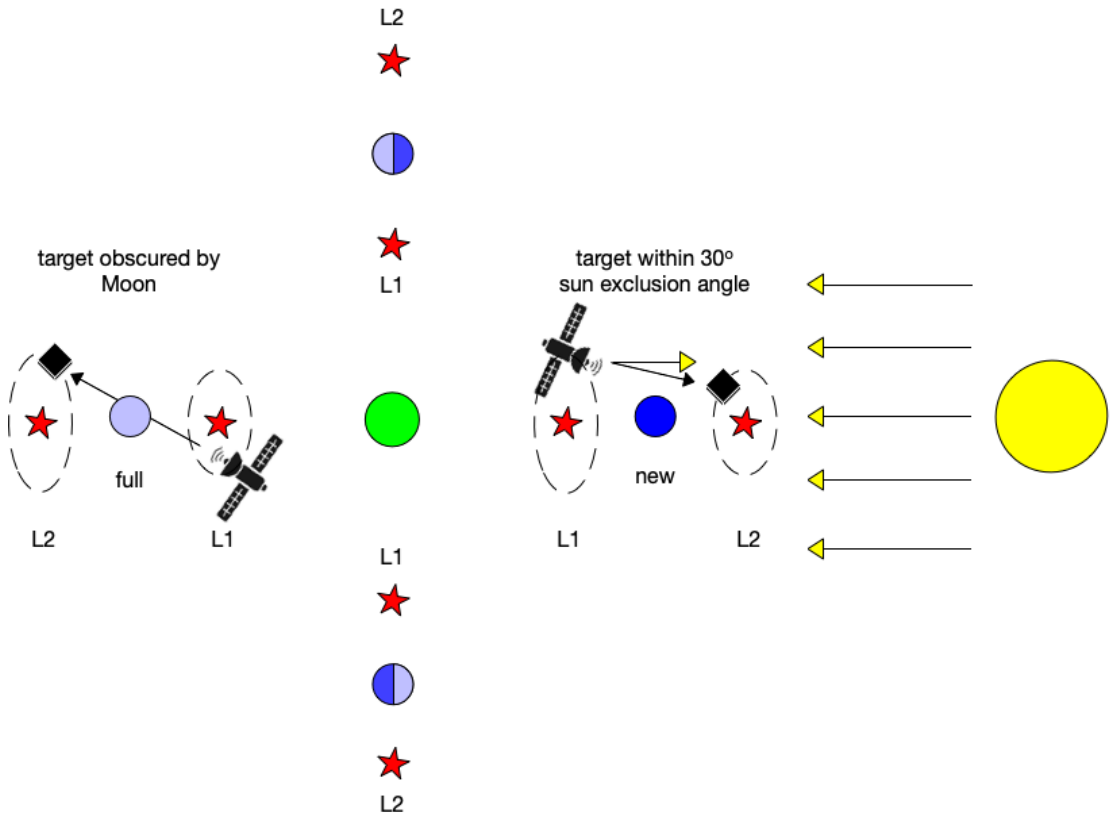

Figure 6: Depiction of Sun-Earth-Moon geometry during different Moon phases. Additionally, on the left is an illustration of inavailability due to obscuration of a target by the Moon from an observer's perspective, and on the right is an illustration of inavailability due to a target's placement within a 30^o sun exclusion angle for an optical sensor. This depiction is simplified since the Sun is actually not quite in the same plane as the Earth-Moon system, which is inclined by 5.145^o with respect to the ecliptic plane.

were varied across the range of values for each parameter. The nominal orbits (using nominal values in Table 2) are shown in bold in the previous visualizations of these orbits (Figure 4, 5). Lyapunov orbits about L1 and L2 were generated according to Broucke.[19] Halo orbits about L1 and L2 were generated according to Richardson.[20] A class I halo is defined by Richardson to be a halo where the $+z$ up part of the halo tilts toward $-x$, and a class II halo is defined by Richardson to be a halo where the $+z$ up part of the halo tilts toward $+x$. Periodic trajectories about L4 were generated according to Grebow.[21] We used a one-hour time step in all cases. Trajectories were integrated using the Matlab ordinary differential equation solver ODE15s over a year for those trajectories that are sufficiently stable and for a single orbit period for unstable trajectories. Those observer trajectories that were propagated for a single orbit period were then repeated in the synodic frame to produce one year of a closed orbit. One year is a sufficiently long period of time to produce a generalized result, independent of epoch. The geometry of the Moon, Earth, and Sun evolves over time, exhibiting periodic behavior over a lunar synodic month (29.5 days), but the lunar orbital plane is inclined with respect to the ecliptic plane by 5.145^o. Thus, without accounting for precession, it takes one year

to observe all possible relative geometries.[9] We consider target and observer orbits that have different periods, all of which are less than a year, thus incorporating small shifts in phasing for target-observer pairings over the course of the year of analysis. Further research into these metrics could incorporate comprehensive phasing scans for target-observer pairings.

Table 2: Orbit families and their defining parameters. *Non-dim* indicates that length is given in non-dimensionalized units (divided by the average distance between the Earth and the Moon). Position components x, y, and z for the Lagrange point orbits are given in the Earth-Moon rotating frame.

Orbit Family	Parameters	Parameter Range	Nominal Value
Keplerian Earth	semi-major axis a	$8378 - 42378$ (km)	25378
	eccentricity e	$0 - 0.5$ (unitless)	0.05
	inclination i	$0 - 90$ (deg)	45
Keplerian Moon	semi-major axis a	$1837 - 2937$ (km)	2387
	eccentricity e	$0 - 0.25$ (unitless)	0.05
	inclination i	$0 - 90$ (deg)	45
L1 Lyapunov	initial state (position component x)	$0.643 - 0.809$ (non-dim)	0.711
L2 Lyapunov	initial state (position component x)	$1.178 - 1.359$ (non-dim)	1.253
L1 Halo	amplitude in z	$1000 - 5500$ (km)	3000
	class	I or II (unitless)	1
L2 Halo	amplitude in z	$1000 - 5500$ (km)	3000
	class	I or II (unitless)	1
L4 Planar	initial state (position component x)	$0.5572 - 0.9203$ (non-dim)	0.727

Figure 7 summarizes the observability results for pairings of observer orbits and target orbits. Range and angular interval are expected to follow a trend similar to that of the empirical observability metric since range and direction are incorporated in the measurement vector definition for the empirical observability calculation. Inavailability is included in the empirical observability metric in that measurements that are unavailable at a given time are not included in the empirical observability matrix calculation.

Numerical observability provides fairly consistent results within each target orbit family. Results are presented as percent improvement over an Earth observer for each target. L2 halo target orbits are 37-65$\%$ more observable by observers orbiting the Moon and Lagrange points than by Earth-orbiting observers, and L1 Lyapunov target orbits are 10-71$\%$ more observable by observers orbiting the Moon and Lagrange points than by Earth-orbiting observers. According to the numerical observability metric, the best observer of the L2 halo orbit family is another L2 halo, and this result matches predictably good results for range and angular interval when an L2 halo observer is tasked to collect observations of an L2 halo target. The best observer of the L1 Lyapunov orbit family is an L4 planar orbit.

L2 Lyapunov target orbits are less observable (between 56% and 200% less) by observers orbiting the Moon and

Lagrange points than by Earth-orbiting observers. L1 halo target orbits are generally less observable (as much as 141% less) by observers orbiting the Moon and Lagrange points than by Earth-orbiting observers, but for two types of observers (L1 halo and L1 Lyapunov), L1 halo target orbits are slightly more observable (up to 20% more observable).

L4 planar target orbits are generally between 3% and 20% more observable by observers orbiting the Moon and Lagrange points than by Earth-orbiting observers, but in the case of an L2 Lyapunov observer, the L4 planar target orbit family is 63% less observable than by an Earth-orbiting observer. L2 halo observer orbits and L1 Lyapunov observer orbits provide the best observations of L4 planar targets according to numerical observability, despite their mediocre to poor performance in the heuristic metrics.

There is no single observer orbit family that solves the cislunar space domain awareness challenge. The results of this analysis motivate the development of a network of space-based sensors in different cislunar orbits. For instance, such a network might include an Earth-orbiting observer, an L2 halo orbiting observer to best observe other L2 halos and to increase capability to observe L1 Lyapunov and L4 planar targets, an L4 planar orbiting observer to provide geometric diversity and to best observe L1 Lyapunov orbiting targets, as well as increasing observations of L2 halos, and an L1 Lyapunov orbiting observer to provide better observations of targets in L1 halo orbits. In the next section we present a method for calculating observability of a cislunar target for a constellation of cislunar observers.

From our analysis we cannot definitively derive consistent trends to connect the numerical observability metric to the heuristic metrics. The heuristic metrics do not take into account the underlying dynamics of the system. The observability metric acknowledges the chaotic nature of the CR3BP for most initial conditions by measuring the extent to which small perturbations to the initial conditions of a given trajectory create changes that appear in the available measurements, supporting its use in further examinations of multiple observers.

Performance Evaluation of Constellations of Cislunar Observers

We calculated the empirical observability metric for two observers using the same process as defined above except that we load two observer trajectories from our catalog and define measurement $\mathbf{y}$ at each time step as an 8×1 vector concatenation of the following quantities: the 3×1 unit vector direction to the target from the first observer, the scalar range between the target and first observer, the 3×1 unit vector direction to the target from the second observer, and the scalar range between the target and second observer. The process may thus also be scaled to observer constellations with more than two spacecraft in future work.

Figure 9 summarizes the observability results for pairings of observer orbits against an L1 Lyapunov target orbit. These results are shown as the percent improvement in empirical observability over the worst-performing observer pairing, which for the L1 Lyapunov target is a constellation of two Earth-orbiting observers. Constellations of observers that include an L4 orbit provide the most improvement in observability for the L1 Lyapunov target.

Figure 10 summarizes the observability results for pairings of observer orbits against an L2 Lyapunov target orbit.

Observer orbit family	Target orbit family: L1 halo		L2 halo		L1 Lyapunov		L2 Lyapunov		L4 planar	
Keplerian Moon	83%	37%	85%	43%	64%	72%	74%	76%	-5%	-923%
	-15%	-82%	-14%	46%	-29%	16%	-8%	-115%	-21%	6%
L1 halo	99%	-52%	74%	-435%	65%	-484%	69%	-776%	1%	-3390%
	98%	8%	0%	37%	-14%	20%	-8%	-157%	14%	11%
L2 halo	64%	-615%	99%	-17%	56%	-1130%	72%	-345%	-15%	-4962%
	25%	-141%	88%	65%	-21%	31%	31%	-106%	21%	13%
L1 Lyapunov	67%	-419%	67%	-736%	57%	67%	57%	-515%	0%	-2434%
	50%	20%	24%	51%	7%	54%	-8%	-158%	-29%	20%
L2 Lyapunov	60%	-716%	77%	-266%	47%	-863%	68%	-391%	-13%	-4749%
	35%	-119%	38%	54%	0%	10%	-38%	-56%	21%	-63%
L4 planar	-62%	15%	-36%	-47%	-47%	35%	-44%	-28%	25%	43%
	30%	-88%	29%	49%	7%	71%	-23%	-200%	0%	3%

Key:	minimum		midpoint		maximum
	range (% avg Earth-Moon distance)			angular interval (% day)	
	inavailability (% simulation time)			empirical observability	

Figure 7: Performance for observer-target pairings against the proposed metrics, shown as percent improvement over an Earth observer for the given target. Each target and observer pair has four values, described in the key.

These results are shown as the percent improvement in empirical observability over the worst-performing observer pairing, which for the L2 Lyapunov target is a constellation of two observers in L4 planar orbits. Constellations of observers that include an L2 Lyapunov orbit provide the most improvement in observability for the L2 Lyapunov target.

Figure 11 summarizes the observability results for pairings of observer orbits against an L4 target orbit. These results are shown as the percent improvement in empirical observability over the worst-performing observer pairing, which for the L4 target is a constellation of two observers in L2 orbits (one in an L2 halo and another in an L2 Lyapunov orbit). Constellations of observers that include an Earth or L1 Lyapunov orbit provide the most improvement in observability for the L4 target.

Figure 12 summarizes the observability results for pairings of observer orbits against an L1 halo target orbit. These results are shown as the percent improvement in empirical observability over the worst-performing observer pairing, which for the L1 halo target is a constellation of two observers in L2 Lyapunov orbits. Constellations of observers that include an Earth or L1 Lyapunov orbit provide the most improvement in observability for the L1 halo target.

Figure 13 summarizes the observability results for pairings of observer orbits against an L2 halo target orbit. These results are shown as the percent improvement in empirical observability over the worst-performing observer pairing,

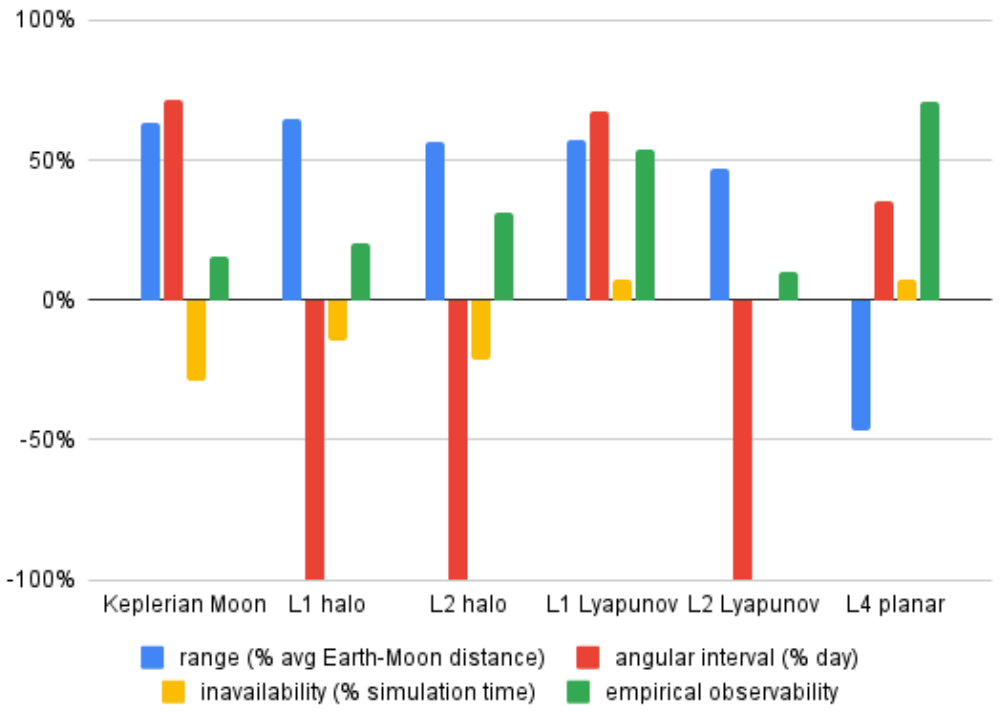

Figure 8: A subset of the values from Figure 7, showing just the results for the various observer orbit families against the L1 Lyapunov target orbit family. The y axis is truncated at -100% for readability.

	Observer orbit family 2						
	Keplerian Earth	Keplerian Moon	L1 halo	L2 halo	L1 Lyapunov	L2 Lyapunov	L4 planar
Observer orbit family 1							
Keplerian Earth	0.0%	72.3%	72.7%	74.7%	70.6%	72.2%	87.1%
Keplerian Moon		77.5%	76.0%	79.7%	75.4%	78.0%	88.3%
L1 halo			74.6%	78.4%	74.8%	76.8%	87.2%
L2 halo				82.2%	78.2%	81.3%	89.7%
L1 Lyapunov					86.4%	76.3%	88.0%
L2 Lyapunov						79.8%	89.6%
L4 planar							88.5%

Figure 9: Empirical observability results for constellations of two observers against an L1 Lyapunov target orbit, shown as the percent improvement over the worst-performing observer pairing (here, two observers in Earth orbits). Results are averages of the results for four different relative geometries, with sun positions at each season of the year. Family nominal values from Table 2 are used to define these observer orbits.

which for the L2 halo target is a constellation of two observers in Earth orbits. Constellations of observers that include an L4 orbit provide the most improvement in observability for the L2 halo target.

Figure 14 summarizes the observability results for pairings of observer orbits against all target orbits. These results are shown as the percent improvement in empirical observability over the worst-performing observer pairing for the given target (denoted by the column title), but the coloring of the cells represents the performance of that pairing of

	Observer orbit family 2						
	Keplerian Earth	Keplerian Moon	L1 halo	L2 halo	L1 Lyapunov	L2 Lyapunov	L4 planar
Observer orbit family 1							
Keplerian Earth	65.7%	55.5%	54.9%	58.2%	53.9%	80.7%	54.0%
Keplerian Moon		33.5%	39.6%	40.4%	36.1%	80.2%	36.1%
L1 halo			37.1%	44.7%	25.5%	80.4%	28.0%
L2 halo				39.2%	42.8%	82.9%	41.3%
L1 Lyapunov					64.1%	81.3%	8.6%
L2 Lyapunov						35.5%	83.2%
L4 planar							0.0%

Figure 10: Empirical observability results for constellations of two observers against an L2 Lyapunov target orbit, shown as the percent improvement over the worst-performing observer pairing (here, two observers in L4 planar orbits). Results are averages of the results for four different relative geometries, with sun positions at each season of the year. Family nominal values from Table 2 are used to define these observer orbits.

	Observer orbit family 2						
	Keplerian Earth	Keplerian Moon	L1 halo	L2 halo	L1 Lyapunov	L2 Lyapunov	L4 planar
Observer orbit family 1							
Keplerian Earth	90.3%	91.0%	90.9%	91.8%	91.3%	89.2%	87.7%
Keplerian Moon		74.9%	61.3%	82.9%	91.1%	75.3%	87.0%
L1 halo			60.0%	89.5%	90.5%	76.4%	87.3%
L2 halo				82.9%	91.3%	0.0%	87.4%
L1 Lyapunov					89.7%	86.8%	88.7%
L2 Lyapunov						65.5%	84.6%
L4 planar							84.7%

Figure 11: Empirical observability results for constellations of two observers against an L4 planar target orbit, shown as the percent improvement over the worst-performing observer pairing (here, two observers in L2 orbits). Results are averages of the results for four different relative geometries, with sun positions at each season of the year. Family nominal values from Table 2 are used to define these observer orbits.

	Observer orbit family 2						
	Keplerian Earth	Keplerian Moon	L1 halo	L2 halo	L1 Lyapunov	L2 Lyapunov	L4 planar
Observer orbit family 1							
Keplerian Earth	62.0%	58.6%	63.6%	55.6%	70.0%	57.3%	57.0%
Keplerian Moon		36.3%	43.5%	20.9%	61.2%	26.9%	30.8%
L1 halo			56.7%	37.0%	68.1%	26.6%	44.0%
L2 halo				6.5%	58.0%	14.5%	21.9%
L1 Lyapunov					55.0%	60.9%	59.9%
L2 Lyapunov						0.0%	24.7%
L4 planar							54.6%

Figure 12: Empirical observability results for constellations of two observers against an L1 halo target orbit, shown as the percent improvement over the worst-performing observer pairing (here, two observers in L2 Lyapunov orbits). Results are averages of the results for four different relative geometries, with sun positions at each season of the year. Family nominal values from Table 2 are used to define these observer orbits.

an observer constellation with a target as compared to the overall worst-performing scenario, which is a pair of Earth-orbiting observers with an L2 halo target. Observability is shown to be very target-dependent, with the L4 planar and L2 Lyapunov orbits more observable than the other cislunar targets and L2 halo targets the least observable. Figure

	Observer orbit family 2						
	Keplerian Earth	Keplerian Moon	L1 halo	L2 halo	L1 Lyapunov	L2 Lyapunov	L4 planar
Observer orbit family 1							
Keplerian Earth	0.0%	37.5%	29.8%	56.0%	53.3%	53.4%	67.6%
Keplerian Moon		54.8%	52.1%	68.7%	66.2%	67.8%	75.9%
L1 halo			47.0%	64.6%	62.1%	64.0%	72.9%
L2 halo				71.2%	71.9%	73.8%	79.4%
L1 Lyapunov					69.9%	70.6%	78.0%
L2 Lyapunov						70.2%	79.2%
L4 planar							82.6%

Figure 13: Empirical observability results for constellations of two observers against an L2 halo target orbit, shown as the percent improvement over the worst-performing observer pairing (here, two observers in Earth orbits). Results are averages of the results for four different relative geometries, with sun positions at each season of the year. Family nominal values from Table 2 are used to define these observer orbits.

18 summarizes single-observer results and also indicates the best second observer to add to a constellation in order to observe a target in a particular orbit.

After determining for each target orbit which pairing of orbit families shows the highest performance according to the empirical observability metric, we explored the range of values that the parameters defining those two observer orbit families could have. Figures 15-17 show that, for all observer orbits that are planar in the CR3BP, larger observing orbits tend to provide better observability, although the performance of sensors in larger orbits may also be negatively affected by large ranges and reduced signal-to-noise ratio. Recall from Figure 15.b that for an L2 Lyapunov orbiting target, the two highest performing observer families are another L2 Lyapunov observer and an L4 planar observer. The highest performing choices within these families are an L4 observer with initial non-dimensional x value 0.5837 and an L2 Lyapunov observer with initial non-dimensional x value 1.2533, which is the same orbit that is being observed, shifted in time. For L4 planar orbits, a higher value of initial x indicates a smaller orbit shape which remains closer to the Lagrange point, and for L2 Lyapunov orbits, a smaller value of initial x indicates a smaller orbit shape in the y direction which remains closer to the Lagrange point. (See Figure 4.) Thus we have found that a larger L2 Lyapunov orbit and a larger L4 planar orbit provide better observability for an L2 Lyapunov target by contributing the greatest geometric diversity in their observations over time. This finding does not hold with an observer in an out-of-plane orbit like a halo. Figure 15.c shows that for an L4 planar orbiting target, the two highest performing observer families are an L2 halo observer and an L1 Lyapunov observer. The highest performing choices within these families are an L2 halo observer with a 1000 km z amplitude and an L1 Lyapunov observer with initial non-dimensional x value 0.6433. Thus here we have found that the smallest L2 halo orbit combined with the largest L1 Lyapunov orbit considered here provide better observability for an L4 planar target. Finally, Figure 15.a presents a banded pattern across the range of L4 planar orbiting observer sizes for an L1 Lyapunov orbiting target. Future study into this phenomenon, which could include developing a larger catalog of orbits with smaller increments between parameter values, may reveal

	Target family				
	L1 halo	L2 halo	L1 Lyapunov	L2 Lyapunov	L4 planar
Observer orbit families					
Keplerian Earth + Keplerian Earth	62%	0%	0%	66%	90%
Keplerian Earth + Keplerian Moon	59%	37%	72%	56%	91%
Keplerian Earth + L1 halo	64%	30%	73%	55%	91%
Keplerian Earth + L2 halo	56%	56%	75%	58%	92%
Keplerian Earth + L1 Lyapunov	70%	53%	71%	54%	91%
Keplerian Earth + L2 Lyapunov	57%	53%	72%	81%	89%
Keplerian Earth + L4 planar	57%	68%	87%	54%	88%
Keplerian Moon + Keplerian Moon	36%	55%	77%	34%	75%
Keplerian Moon + L1 halo	43%	52%	76%	40%	61%
Keplerian Moon + L2 halo	21%	69%	80%	40%	83%
Keplerian Moon + L1 Lyapunov	61%	66%	75%	36%	91%
Keplerian Moon + L2 Lyapunov	27%	68%	78%	80%	75%
Keplerian Moon + L4 planar	31%	76%	88%	36%	87%
L1 halo + L1 halo	57%	47%	75%	37%	60%
L1 halo + L2 halo	37%	65%	78%	45%	90%
L1 halo + L1 Lyapunov	68%	62%	75%	26%	91%
L1 halo + L2 Lyapunov	27%	64%	77%	80%	76%
L1 halo + L4 planar	44%	73%	87%	28%	87%
L2 halo + L2 halo	6%	71%	82%	39%	83%
L2 halo + L1 Lyapunov	58%	72%	78%	43%	91%
L2 halo + L2 Lyapunov	15%	74%	81%	83%	0%
L2 halo + L4 planar	22%	79%	90%	41%	87%
L1 Lyapunov + L1 Lyapunov	55%	70%	86%	64%	90%
L1 Lyapunov + L2 Lyapunov	61%	71%	76%	81%	87%
L1 Lyapunov + L4 planar	60%	78%	88%	9%	89%
L2 Lyapunov + L2 Lyapunov	0%	70%	80%	35%	66%
L2 Lyapunov + L4 planar	25%	79%	90%	83%	85%
L4 planar + L4 planar	55%	83%	89%	0%	85%

Figure 14: Summary of empirical observability results. The number in each cell is the percent improvement over the worst-performing two-observer constellation against the specific target in that column title. The entry representing the best improvement in a column is emphasized by a black outline. The color of the cell represents the performance of that two-observer constellation against that target as compared to the worst-performing combination of a two-observer constellation with any target shown in the matrix. (Here, the worst-performing combination is two Earth-orbiting observers with an L2 halo target.) Family nominal values from Table 2 are used to define these observer orbits.

more details about this apparent frequency interference between the L4 planar orbiting observer and its L1 Lyapunov orbiting target.

CONCLUSION

The viability of Keplerian and cislunar orbit families for cislunar space domain awareness has been evaluated using heuristic metrics and an empirical observability metric. Application of nonlinear observability theory to the cislunar

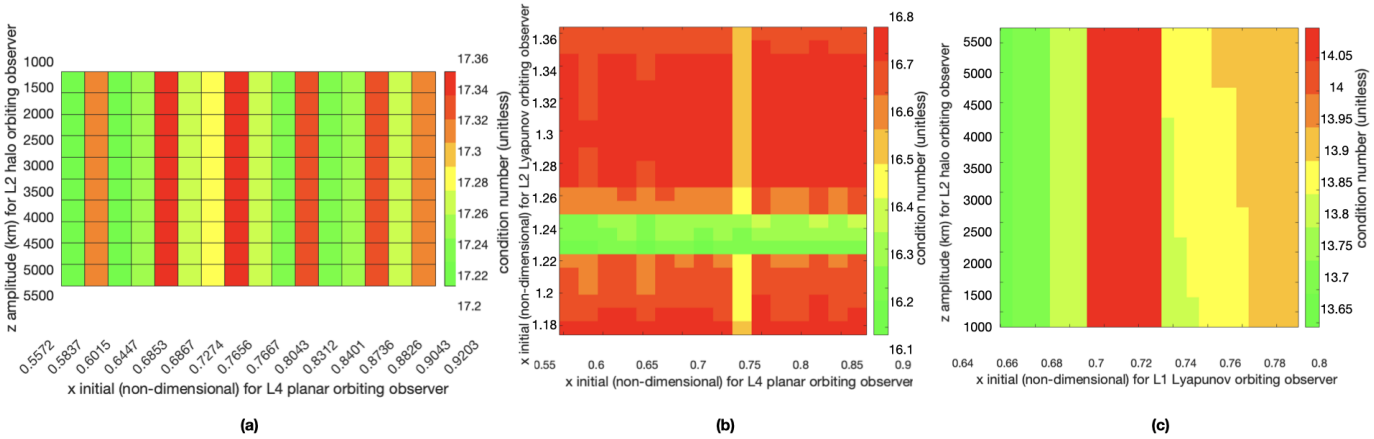

Figure 15: Parameter optimization results for (from left to right) the two highest performing observer families for an L1 Lyapunov orbiting target, an L2 Lyapunov orbiting target, and an L4 planar orbiting target.

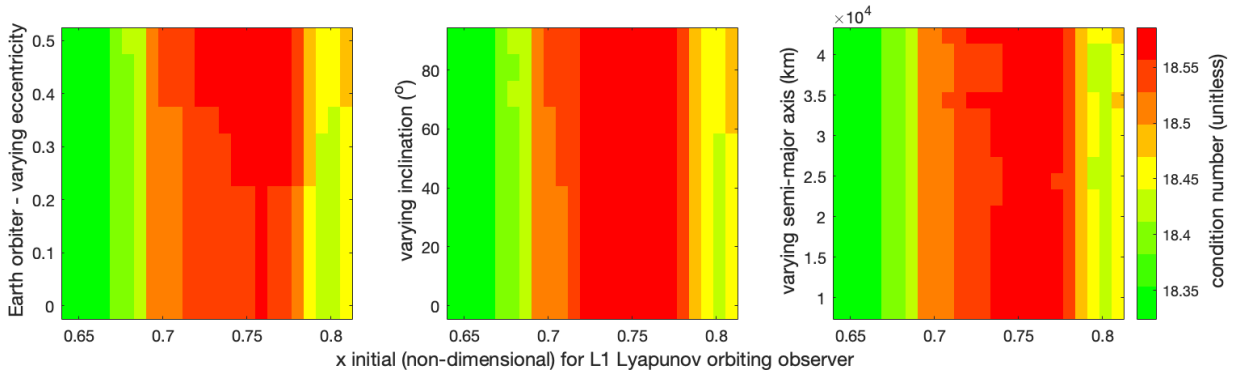

Figure 16: Parameter optimization results for the two highest performing observer families for an L1 halo orbiting target.

space domain awareness problem has shown that L2 halo target orbits are particularly difficult to observe, and L4 planar orbits particularly observable. Although the range heuristic for L4 planar orbits reflects the large range between L4 and other parts of cislunar space, these orbits are shown to be high-performing in observer constellations for the L1 Lyapunov target, the L4 planar target, and the L2 halo target. This analysis advances research in the fields of cislunar dynamics and observability so as to support the selection of effective orbits for satellites that may be launched in the near future to accomplish the space-based cislunar domain awareness mission. Future work includes extending the empirical observability results to include constellations of three or more observers from various of the orbit families described here and considering the ΔV required for station-keeping in these orbits in order to further evaluate the viability of these orbits for cislunar SDA missions. Another worthy subject for future work might be to consider alternate methods for sampling various phasing for celestial bodies as well as observers and target.

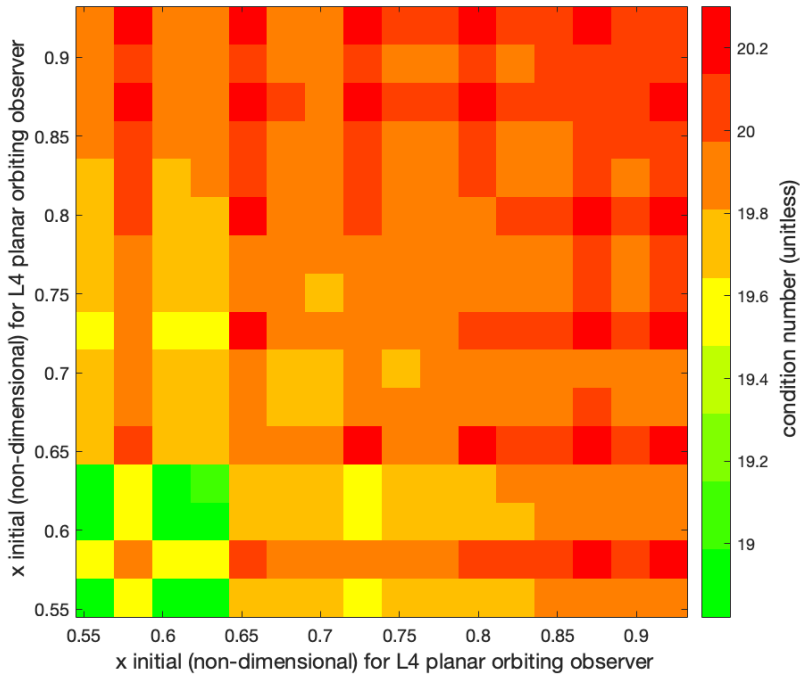

Figure 17: Parameter optimization results for the two highest performing observer families for an L2 halo orbiting target.

ACKNOWLEDGMENTS

Stella Hurtt co-authored the preliminary version of this paper which appeared at the 31st AAS/AIAA Space Flight Mechanics Meeting in February 2021. E. Fowler was supported in part by the U.S. Naval Research Laboratory Edison Memorial Graduate Training Program.

CONFLICT OF INTEREST STATEMENT

On behalf of all authors, the corresponding author states that there is no conflict of interest.

REFERENCES

[1] S. Lizy-Destrez, L. Beauregard, E. Blazquez, S. Manglativi, and V. Quet, "Rendezvous Strategies in the Vicinity of Earth-Moon Lagrangian Points," *Frontiers in Astronomy and Space Sciences*, Vol. 5, 2019, pp. 1–19, 10.3389/fspas.2018.00045.

[2] D. Folta and F. Vaughn, "A Survey of Earth-Moon Libration Orbits: Stationkeeping Strategies and Intra-Orbit Transfers," *Proceedings of the AIAA/AAS Astrodynamics Specialist Conference and Exhibit*, No. AIAA 2004-4741, 2004.

[3] M. R. Bobskill and M. L. Lupisella, "The Role of Cis-Lunar Space in Future Global Space Exploration," *Proceedings of the Global Space Exploration Conference*, Washington, District of Columbia, 2012, pp. 1–15. May 22–24, 2012. Paper number GLEX-2012.05.5.4x12270.

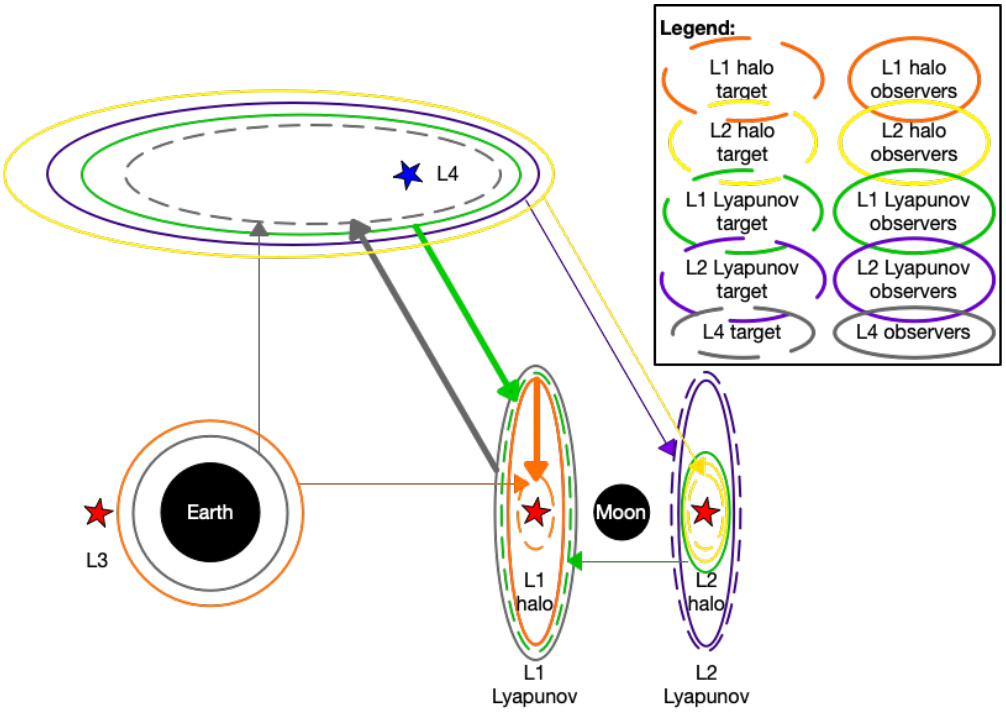

Figure 18: Summary of results. Target trajectories are shown as dashed lines, and observer trajectories are shown as solid lines. Matching colors represent high-performing observer-target pairings. Thick arrows represent the best single observers according to empirical observability results, and thin arrows represent the best second observer to add to the constellation for a given target according to multi-observer empirical observability results. For instance, in green the best single observer for an L1 Lyapunov target is an L4 orbit, and an L2 halo is the best second observer to add to the constellation. In the case of an L2 Lyapunov target and an L2 halo target, the best single observer is another trajectory of the same type.

[4] J. Chase, N. Chow, E. Gralla, and N. J. Kasdin, "LEO Constellation design using the lunar L1 point," *Proceedings of the 14th AAS/AIAA Space Flight Mechanics Meeting*, Maui, HI, 2004, pp. 1–19. February 8–12, 2004. Paper number AAS 04-248.

[5] T. A. Pavlak and K. C. Howell, "Evolution of the Out-of-Plane Amplitude for Quasi-Periodic Trajectories in the Earth-Moon System," *Acta Astronautica*, Vol. 81, No. 2, 2012, pp. 456–465.

[6] B. L. Jones, *A Guidance and Navigation System For Two Spacecraft Rendezvous in Translunar Halo Orbit*. PhD thesis, University of Texas at Austin, Austin, TX 78712, 5 1993.

[7] R. S. Park and A. B. Chamberlin, "Jet Propulsion Laboratory Horizons Database," `https://ssd.jpl.nasa.gov/horizons.cgi`.

[8] A. J. Krener and K. Ide, "Measures of Unobservability," *Proceedings of the 48th IEEE Conference on Decision and Control (CDC) held jointly with the 2009 28th Chinese Control Conference*, Shanghai, China, 2009, pp. 6401–6406.

[9] S. R. Knister, "Evaluation Framework for Cislunar Space Domain Awareness (SDA) Systems," Master's thesis, Air Force Institute of Technology, Wright-Patterson Air Force Base, Ohio, 2020. 3243. AFIT-ENV-MS-20-M-221.

[10] W. S. Koon, M. W. Lo, J. E. Marsden, and S. D. Ross, *Dynamical Systems, the Three-Body Problem and Space Mission Design*. Springer, 2007.

[11] J. M. A. Danby, *Fundamentals of Celestial Mechanics*. Willmann-Bell, 2nd ed., 1992.

[12] A. E. Roy, *Orbital Motion*. Taylor & Francis Group, 4th ed., 2005.

[13] J. S. Parker and R. L. Anderson, *Low-Energy Lunar Trajectory Design*. Wiley, 1st ed., 6 2014.

[14] G. Gomez, J. Llibre, R. Martinez, and C. Simo, *Dynamics and Mission Design Near Libration Points, Fundamentals: The Case of Collinear Libration Points*, Vol. 2 of *World Scientific Monograph Series in Mathematics*. World Scientific Publishing, 4 2001.

[15] R. R. Bate, D. D. Mueller, and J. E. White, *Fundamentals of Astrodynamics*. Dover, 1971.

[16] M. Beckman, "Orbit Determination Issues for Libration Point Orbits," *Proceedings of the International Conference of Libration Point Orbits and Applications*, Girona, Spain, 2002, pp. 1–9. June 10–14, 2002. Paper number 20020081023.

[17] E. Kaufman, T. A. Lovell, and T. Lee, "Nonlinear Observability for Relative Orbit Determination with Angles-Only Measurements," *Journal of Astronautical Sciences*, Vol. 63, 2016, pp. 60–80. 10.1007/s40295-015-0082-9.

[18] D. A. Vallado, *Fundamentals of Astrodynamics and Applications*. Microcosm Press and Kluwer Academic Publishers, 2nd ed., 2001.

[19] R. A. Broucke, "Periodic Orbits in the Restricted Three-Body Problem with Earth-Moon Masses," Tech. Rep. 321168, Jet Propulsion Laboratory, Pasadena, CA, February 1968.

[20] D. L. Richardson, "Analytic Construction of Periodic Orbits about the Collinear Points," *Celestial Mechanics*, Vol. 22, 1980, pp. 241–253.

[21] D. J. Grebow, "Generating Periodic Orbits in the Circular Restricted Three-Body Problem with Applications to Lunar South Pole Coverage," Master's thesis, Purdue University, West Lafayette, IN, May 2006.